In-situ CT damage analysis of metal inserts embedded in carbon fiber-reinforced plastics

F. Pottmeyer, J. Bittner, P. Pinter, Kay A. Weidenmann

Angaben zur Veröffentlichung / Publication details:

Pottmeyer, F., J. Bittner, P. Pinter, and Kay A. Weidenmann. 2017. "In-situ CT damage analysis of metal inserts embedded in carbon fiber-reinforced plastics." *Experimental Mechanics* 57 (9): 1411–22. https://doi.org/10.1007/s11340-017-0312-0.

In-Situ CT Damage Analysis of Metal Inserts Embedded in Carbon Fiber-Reinforced Plastics

F. Pottmeyer[1] · **J. Bittner**[1] · **P. Pinter**[1] · **K.A. Weidenmann**[1]

Abstract Carbon-fiber-reinforced plastics (CFRPs) are gaining increasing applicability to lightweight structures (e.g., automotive applications) due to their outstanding mechanical properties. High-performance parts can be fabricated from CFRPs, but they have the disadvantages of low shear and bearing strength. To achieve detachable connections and introduce loads without decreasing the load-bearing capacity of the composite, it is important to use mechanical fasteners without drilling into the parts. To accomplish this, metal elements called inserts are embedded in the CFRP laminate. Damage behavior in a CFRP under tensile conditions has several different mechanisms, depending primarily on the deformation of the insert. This research investigates the in-situ failure behavior of the composite under tensile loads by investigating the deformation of the insert via computed tomography (CT). The results are also used for validation of the insert's deformation using a finite-element model (FEM).

Keywords Composite · Joining · Inserts · X-ray computed tomography · Damage evolution

✉ F. Pottmeyer
Florentin.Pottmeyer@kit.edu

J. Bittner
uaerq@student.kit.edu

P. Pinter
Pascal.Pinter@kit.edu

K. A. Weidenmann
Kay.Weidenmann@kit.edu

[1] Karlsruhe Institute of Technology (KIT), Institute for Applied Materials IAM–WK, Kaiserstr. 12, 76131 Karlsruhe, Germany

Introduction

Continuous CFRPs are often used in heavily loaded lightweight structures and are typically thin-walled. Mechanical fasteners can provide an inexpensive, detachable means of connection [1]. Rivets and bolts require that the parts be drilled before fastening, leading to inevitable stress concentrations in the laminate and reduced load bearing capacity of the composite [2–5]. Another joining method involves inserts made of metal sheets with welded bushings. They are embedded in the laminate during preforming, during which the fibers of the plies are not cut but guided around the bolt to maintain fiber continuity [6]. Previous investigations of inserts embedded in CFRP mostly involved evaluating the measured maximum forces for inserts under different loading conditions. Ferret et al. [7] investigated the performance of two different types of bigHead® inserts under tensile (pull-out), bending and pressure (push-in) loads. The inserts had different geometric parameters such as diameter, shape and number of holes in the metal sheet. It was shown that the load bearing capacity was higher for the smaller diameter insert. The failure behavior of the composite, including fiber failure, was described only with post-mortem micrographs. Hopmann et al. [8] compared insert performance to bonded fasteners (so-called onserts) in pull-out tests and found the performance of inserts to be up to 37% better. They also studied the different damage mechanisms using post-mortem photographs. Fleischer et al. [9] studied insert performance under different loading conditions with an improved shape and additional surface treatments. Pins generated by additive manufacturing (SLM) improved the tensile strength up to 42% in their study. Arc-sprayed insert variants enhanced the bending strength up to 41%. The failure behavior, including the failure of the co-cured bonding connection between the insert and the plies, was depicted only with polished cut images. Additionally,

the shapes of the test curves were compared for all insert variants. Schwarz et al. [10, 11] investigated the influence of fiber volume fracture, height of point of application, diameter and thickness of the insert's metal sheet for bending loads. These results were subsequently compared with a mechanical-analytic analogous model and a finite element model (FEM). The model outputs agreed well with the experimental results, enabling the authors to make design recommendations for the construction of embedded inserts. In a preliminary study [12], the current authors tested different types of inserts under various loading conditions and determined the tensile load to be the critical loading case. The load-bearing capacities strongly depended on the thickness of the base plates and the related bending stiffness. The damage behavior was described using optical analysis of post-mortem cut images. The failure types included crosswise fiber breakage around the stud, plastic deformation of the insert and delamination failure of the co-cured bonding. Despite the identification of the failure types, no statement could be provided about the damage evolution of the composite under loading. Computed tomography offers the possibility for evaluating the local laminate quality of FRPs in general; e.g., the determination of the degree of porosity in CFRP laminates [13], or the geometry of fiber bundles and voids in GFRP [14]. In [15], computed tomography was used to examine the distribution of matrix cracks in CFRP specimens after impact loading. Nouri et al. [16] used CT analysis to reveal the connection between shear-induced fiber/matrix debonding and transverse cracking in the evolution of damage in CFRP laminates. Ireman et al. [17] also investigated damage development in mechanically fastened composite laminates using computed tomography. Here, the X-ray images were taken after certain loading sequences, so the load transfer had to be interrupted before scanning the specimen. This inspection showed the presence of delamination and extensive fiber and matrix fracture. In-situ CT is already in use to determine the damage evolution in FRP under different loading conditions. The in-situ deformation behavior of FRP-sandwich structures under compression and impact loads has been successfully researched in [18–20]. In [21], CFRP specimens were tested under compression according to ASTM D 7291, and damage analysis was performed. Other approaches have also used in-situ CT measurements for diagnosing damage in CFRP laminates [22–24], aluminum alloys [25] or SiC/SiC minicomposites [26].

FEM is widely used for damage prediction or to complete experimental studies [27, 28]. The use of cohesive behavior (CB) or cohesive elements (CEs) in combination with different damage criteria is a common method for damage prediction (e.g., de-bonding, interfacial behavior, and delamination) in composites [28]. Aymerich et al. [29] addresses impact-induced delamination in cross-ply composite laminates using CEs and the stress-based quadratic criterion. The FE model correctly predicted the damage mechanisms and locations for a wide range of impact energies. Al-Zand et al. [30] compares three surface interaction techniques (tie interaction, CEs and CB) to simulate the bonding behavior between a steel tube and a CFRP under flexural loads. Delamination failure could not be simulated using tie interactions. However, both the CB and CE models accurately reflect the CFRP experimental results, including both rupture and delamination failures. Simulation and validation of mechanically fastened composite laminates has been previously completed. Kapidžić et al. [31] investigated the bearing failure and strength of a carbon-epoxy laminate and the influence of biaxial bolt load using both CEs and the quadratic stress damage criterion. The results show the bearing failure loads of the simulations and the experiments do not differ significantly. The failure process started with matrix cracking and progressed to fiber kinking failure combined with delamination. Simulated inserts were investigated by Schwarz et al. [10, 11]. Here, the force initiation element was modeled as ideally bonded using the tie functionality, which corresponds to a dramatic simplification of the interface. This technique is sufficient to validate the maximum transmitted force, but does not suitably represent the insert deformation.

In this research, the CFRP-embedded insert was tested under the previously mentioned critical tensile load. The tensile testing machine was installed in the CT machine to get in-situ results at different loads and displacements. This allowed study of the damage evolution of the laminate and deformation mechanism of the insert for the first time. Instead of an optical, post-mortem analysis, it is possible to detect damage mechanisms during the loading conditions. Furthermore, an FE model is developed and validated using the results of the CT scans, including a quantitative deformation analysis of the insert.

Experimental

Materials and Specimen Geometry

The specimen was a flat CFRP plate with dimensions of 150 mm × 150 mm with one centrally positioned metal insert. This type of specimen has been previously tested in [6; 9; 12]. A photograph and diagram showing component dimensions are presented in Fig. 1.

The reinforcement consisted of eight plies of a multiaxial non-woven carbon fiber fabric (Hexcel NLT00 series, 0°/90°, 200 g/m^2) with a high-strength reinforcement yarn. The epoxy resin was manufactured by Sika® (Biresin® CR170/CH150–3). The insert consisted of a flat metal sheet and a threaded bolt and was made of stainless steel (1.4301) to prevent corrosion. During the preforming process, the inserts were embedded between the four lower and four upper plies of the carbon fiber

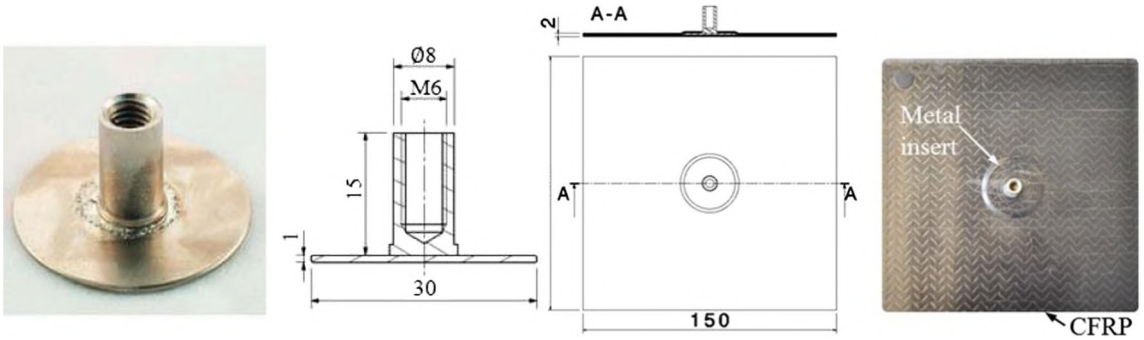

Fig. 1 Photograph and dimensions of the metal inserts and CFRP specimens [9]

fabric. Next, the fibers of the upper plies were guided around the bolt in the insert to maintain fiber continuity. Finally, the specimen was manufactured by the RTM process at the Institute of Production Science (wbk) at KIT with a fiber volume fracture of 0.44 and cured at 70 °C for 90 min. The infiltration of the preform was carried out on a hydraulic press (Lauffer type RP 400) with a flow metering and mixing machine (Tartler Nodopur VS-2 K) at an infiltration pressure of 9 bar.

Test Setup and Procedure

The pull-out test was performed using an electromechanical in-situ testing machine made at IAM-WK which has been previously used in [32]. Figure 2 (a) shows a 3D model and two sections of the machine. The transmission was designed with a worm gear powering a threaded rod. The unloaded specimen was placed on top of the carbon tube with the insert directed downwards. An M6 threaded rod was screwed in the insert's stud. The test was performed with the rod moving down, with the carbon tube serving as a hold-down clamp. The test output consisted of the measured displacement of the threaded rod and the load cell force. To compare the laminate damage results, the diameter of the carbon tube was similar to the pull-out test described in [12]. The crosshead velocity was also set at 1.5 mm/min. The self-locking effect of the worm gear prevented a change of the displacement of the machine after stopping. During the CT scan, neither the machine nor the specimen can be moving.

The experimental setup of the in-situ pull-out test is shown in (Fig. 2 b). The test machine was installed on the rotary plate of the CT machine, which consisted of an X-ray tube (Yxlon) and a detector (PerkinElmer). Beam hardening of the polychromatic x-rays can be reduced by shortening the radiography distance. For that reason, the entire machine was positioned at an incline of 12° (cf. Fig. 2 (b)). Metal filters (e.g., tin) can also be used to sharpen the x-ray spectrum [33]. Accordingly, a small 1-mm-thick tin plate was screwed on the tungsten target of the x-ray tube. The acceleration voltage was set to 200 kV, and the tube current was 0.75 mA. A total of 2430 projections at an exposure time of 500 ms were performed, with a resolution of 46.5 μm/voxel.

Results

Pull-Out Test

Figure 3 shows the force versus displacement curve for the in-situ pull-out test. The shape of the test curve is distinguished by typical progressive damage behavior, characterized by frequent force decreases. According to [12], different types of failure occur during the tensile test. Beside fiber and matrix breakage, failure of the co-cured bonding leads to a detachment of the insert from the laminate and also to plastic deformation of the insert. Delamination primarily appears as the specimen approaches the final failure point. The in-situ scans are depicted with dashed lines. Failure of the specimen was always assumed when a significant force decrease occurs. These forces correspond to the so-called holding forces when the test machine was stopped to complete the CT scan. An exception is at point 1, where no force decrease occurred during the scan. The CT scan started after a short residence time of up to five minutes during which the holding force decreased due to relaxation. At the end of the test, the failed specimen was unloaded and scanned (cf. Figure 3 point 9) to discover the failure types, especially the plastic deformation of the insert. Table 1 gives an overview of the scans and the corresponding holding forces. Each scan has two forces, "Force Machine Stopped" and "Force CT-Scan", the latter of which is always smaller due to relaxation.

Damage Evolution Analysis

With the help of the in-situ CT scan, it is possible to get detailed information about the damage evolution of the compound. An example picture of scans 1 to 3 is shown in Fig. 4. A slight elastic deformation of the insert is observed with increasing force, but no conclusion can be reached regarding the first decrease of force below 2000 N, which may be due to fiber fracture and/or matrix cracking. The co-cured bonding

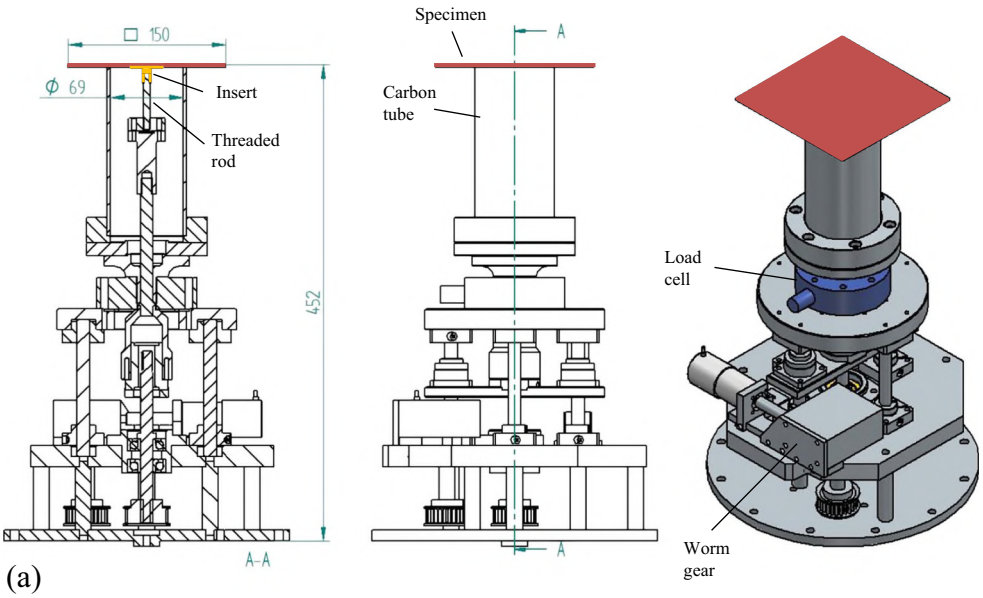

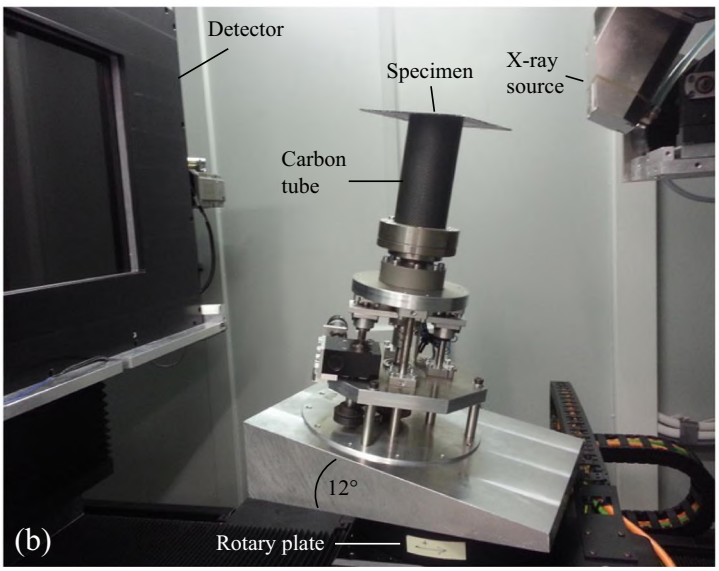

Fig. 2 **a** 3D model and section of the in-situ testing machine with the specimen on top of the carbon tube **(b)** Experimental setup of the in-situ pull-out test.

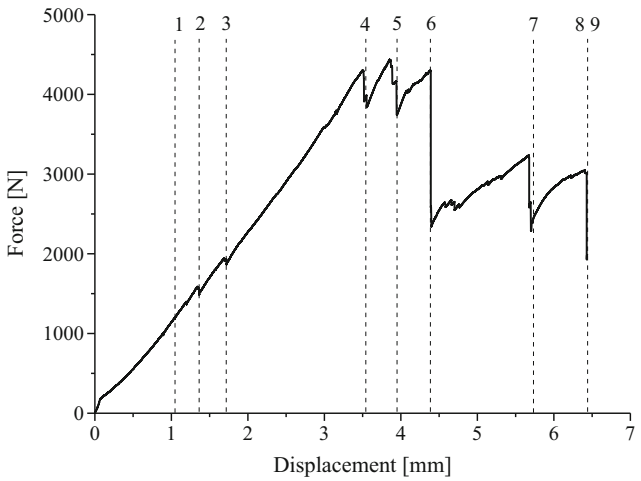

Fig. 3 Results curve of the in-situ pull-out test with stops for CT scans (dashed lines)

Table 1 Number of scans and holding forces

Scan	Force Machine Stopped [N]	Force CT-Scan [N]
1	1380	1366
2	1508	1490
3	1900	1896
4	3970	3838
5	3833	3744
6	2500	2340
7	2555	2287
8	1954	1944
9	0	0

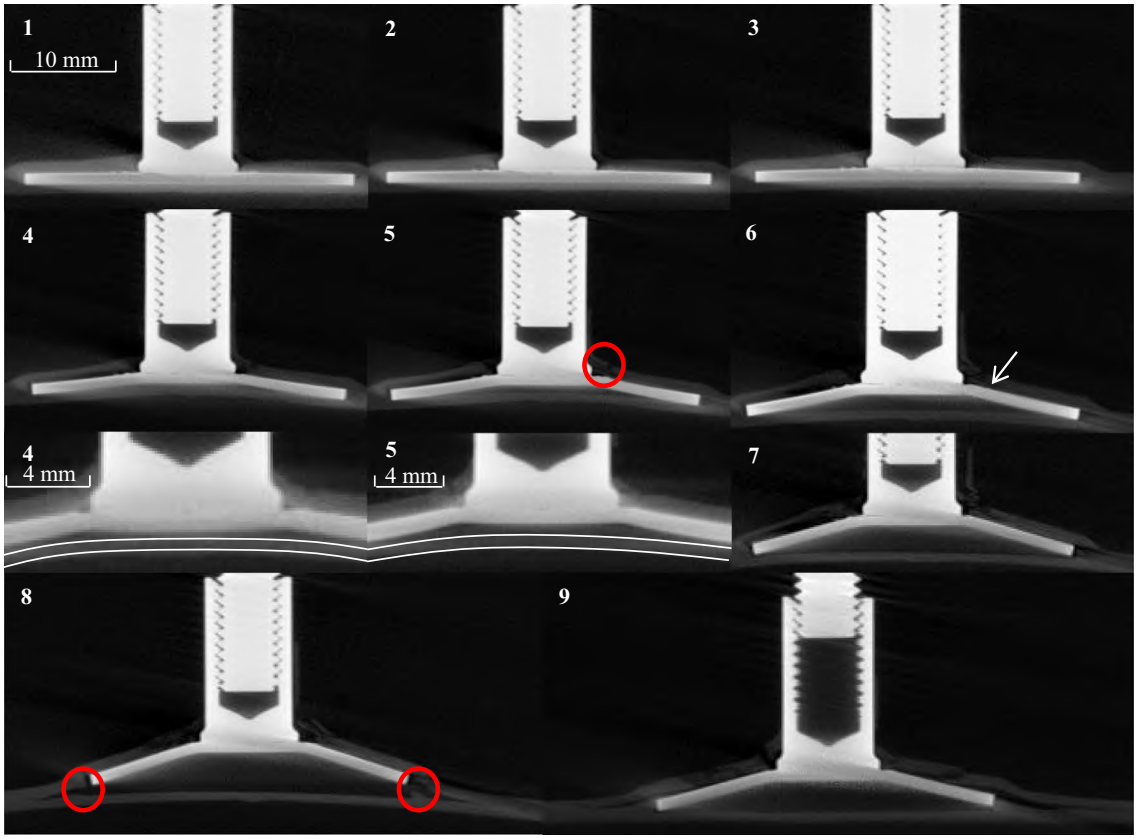

Fig. 4 CT scans 1 (1366 N), 2 (1490 N) and 3 (1896 N) – showing slight elastic deformation of the insert without visible fractures; CT scans 4 (3838 N) and 5 (3744 N) with fiber breakage (*red*) around the stud and co-cured bonding failure and CT scans 6 (2340 N), 7 (2287 N), 8 (1944 N) and 9 (0 N) with fiber breakage and delamination (*red*)

failure and the plastic deformation of the insert can be observed at point 4, where a significant force decrease occurs. In Fig. 4, the lower laminate is marked with a white border to highlight the resulting gap underneath the insert, which grows with increasing force (points 4 to 5). The resulting fiber cracks are caused by the insert's deformation, which leads to stress peaks around the stud. Since the deflection of the insert's metal plate is hampered by the upper CFRP laminate, the deflection curve is nonlinear. The highest force decrease of approximately 2000 N occurred at point 6. As seen in Fig. 4, only a small part of the insert's surface is detached from the laminate. At point 7, the interface between the insert and the laminate is completely separated. The fiber fractures around the stud proceed simultaneously with the detachment of the insert. Furthermore, the shape of the deflection of the boundary metal plate of the insert is now almost linear. This is due to a crack initiation on the upper side of the metal plate (white arrow) at point 6. The insert is completely detached from the laminate at point 8, which leads to delamination between the CFRP plies. A scan of the tested, unloaded specimen can be seen at point 9. The decrease of the insert's deformation caused by the elastically stored energy is clearly visible, and the fiber breakage and delamination is also apparent.

Quantitative Deformation Analysis

The volume of images from the CT scans were post-processed in ImageJ® to separate the insert from the matrix material. A 3D median filter and threshold segmentation were applied. After segmentation, the surface of the insert was measured by a simple in-house developed MATLAB® tool. Starting from the bottom plane of the picture (cf. Fig. 5 (a)), the first voxel inside the insert is found for each point of the plane and stored to a two-dimensional matrix that describes the shape of the surface. Figure 5 (b) shows a 3D plot of the extracted surface. To validate the FEM simulation, a line plot was extracted exactly in the center of the insert (Fig. 5 b) red line).

Figure 5 (c) shows the deformation path of the insert from the beginning of the test until final failure. In the beginning, the deformation is small but continuous. At point 4, the insert begins de-bonding from the CFRP-laminate, which explains the sudden significant increase in the deformation. The deformation increases with increasing force until final failure. As soon as the specimen is unloaded (scans 8 to 9), the restoring force of the elastically stored energy can be observed in the decrease of the deformation path as well as in the expansion of the test curve.

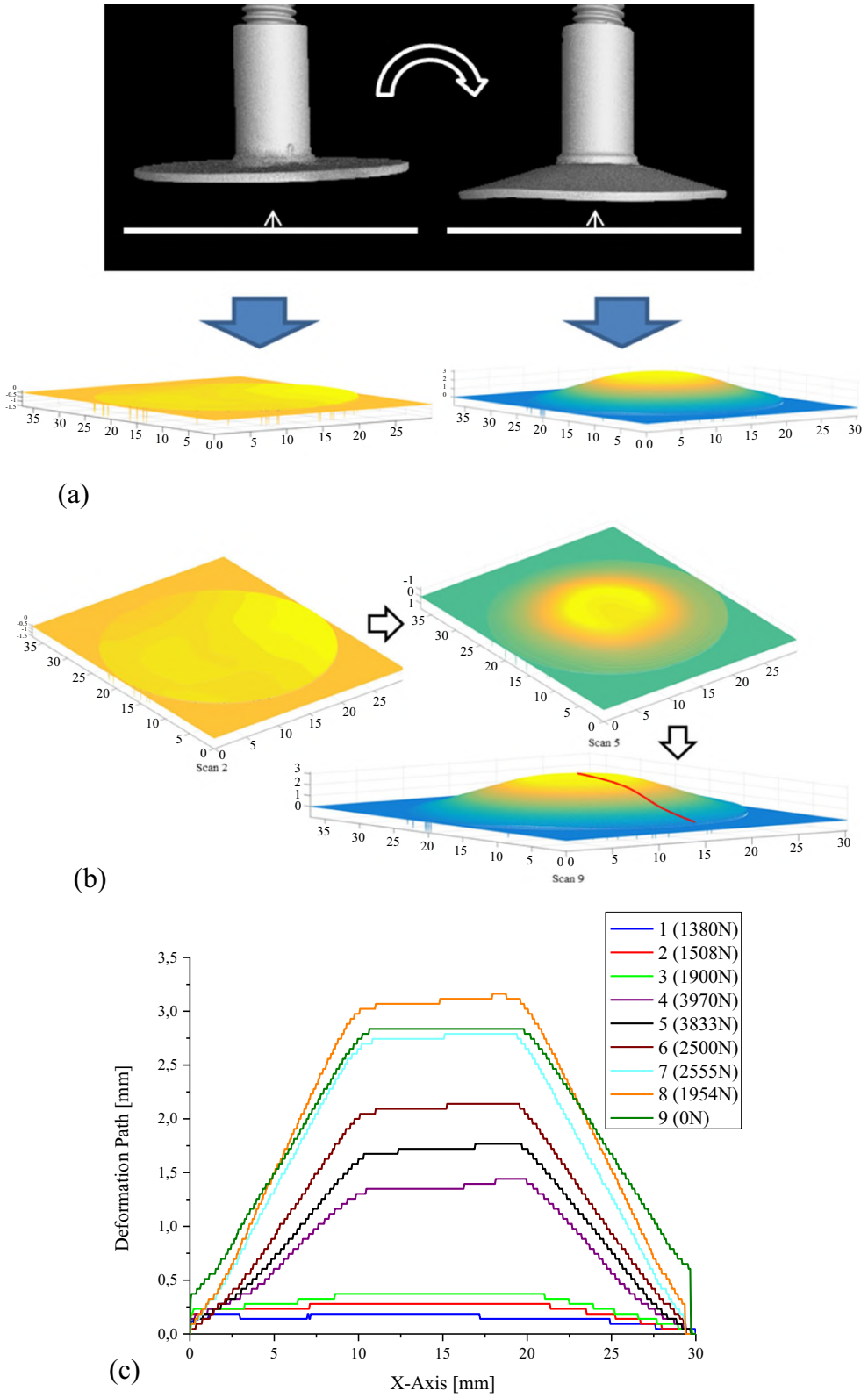

Fig. 5 **a** Illustration of reading the unloaded and tested reconstructed inserts in Matlab® **(b)** Insert deformation development **(c)** Development of the deformation path of the insert

Using the software ABAQUS®, a 3D quarter-section model of the composite was created (cf. Figure 6 (a)). A laminate consisting of 16 single layers was built up using two composite layup functions, described in detail in [34], including 8 unidirectional layers for each of the upper and the lower laminates, and accounting for the fiber orientations. Modeling each individual layer would be too complex and unnecessary because the insert deformation is the region of interest. The

laminate diameter was 69 mm. The pure resin pocket between the edge of the insert and laminate was modeled as an additional chamfer on the insert, using the material properties of the cured resin. The hold-down clamp was modeled by a boundary condition with a constraint applied in the axial (y-) direction. The load was introduced by a displacement-controlled boundary condition in the axial (y-) direction. These conditions were modeled with symmetric boundary conditions in the x- and z-directions (cf. Figure 6 b) and c)). To verify the simplification of the modeled hold-down clamp,

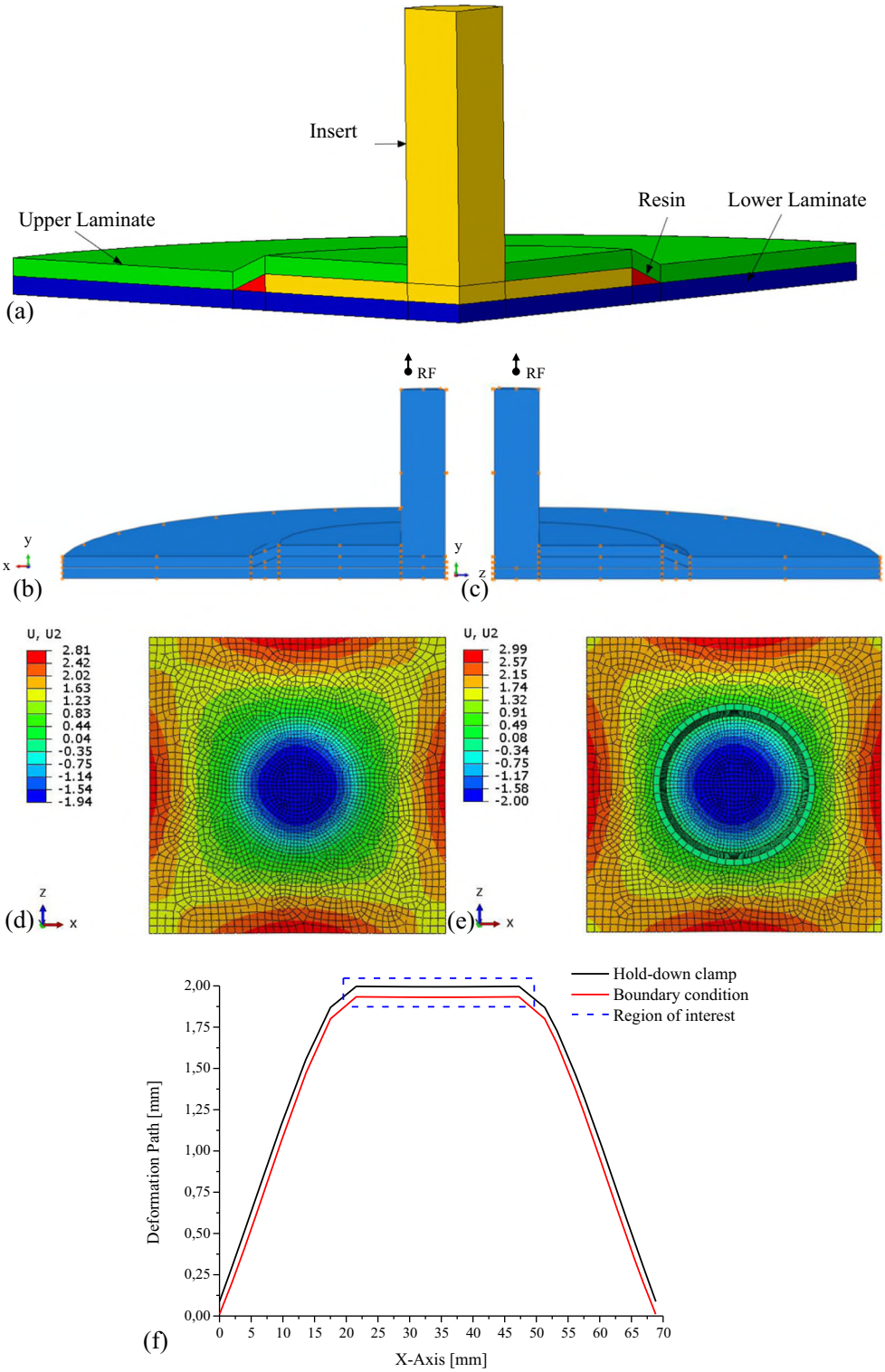

Fig. 6 **a** Quarter-section model of the composite – the pure resin pocket is modeled as a chamfer on the insert **(b)** and **(c)** Symmetric boundary conditions of the model with displacement-controlled load introduction from the insert to the reference point (RF) and fixed degrees of freedom in the y-direction on the outer edge of the laminate **(d)** Y-displacement of a CFRP laminate with fixed degrees of freedom in the y-direction **(e)** Y-displacement of a CFRP laminate with CFRP hold-down clamp **(f)** Comparison of the deformation paths of **(d)** and **(e)** within the diameter of the hold-down clamp

Table 2 Values used for modeling

Model Parameter								
Material	σ_{true} [*MPa*]	ε_{ln}^{pl} [–]	E_1 [*MPa*]	E_2/E_3 [*MPa*]	ν_{12}/ν_{13} [–]	ν_{23} [–]	G_{12}/G_{13} [*MPa*]	G_{23} [*MPa*]
CFRP			107,420	5494	0.281	0.35*	2037	2037*
Steel	199 939	0 0.48	200,000		0.24			
Resin			3000		0.35		1111	
Damage Behavior								
Interface Properties	G_{Ic} [N/mm]	$\{t_n^o\ t_s^o\ t_t^o\}$ [*MPa*]						
Steel/CFRP	0.35 [36]	2.5** 4 [37]*** 4 [37]***						

*Assumed

**Measured with cross tension test

***Measured with shear edge test [37]

the deformation paths of two CFRP composite layups were compared. Therefore, the force was set to 4000 N and introduced into the laminate over an area of the inserts diameter which was 30 mm. In Fig. 6 (d) the hold-down clamp was set similar to the boundary condition of the inserts model (cf. Figure 6 b) and c)). The hold-down clamp of (Fig. 6 e) was modeled as a CFRP tube, whereby the material properties were adopted from the CFRP laminate (cf. Table 2). Both laminates to be compared were built up using 3617 C3D20R elements, while the hold-down clamp was modeled with 560 additional elements. The coefficient of friction CFRP/CFRP needed for the simulation with hold-down clamp was taken from literature [35] and set to 0.65. In Fig. 6 (f) the deformation paths of the x-axis within the diameter of the hold-down clamp of 69 mm are compared for both simulations. The courses of both deformation paths are very similar, whereby the maximum deviation of displacement within the region of interest (inserts diameter of 30 mm) from 19.5 mm to 49.5 mm is approximately 3%. Hence, it can be concluded that the simplification of the hold-down clamp using the boundary condition with constraint in the direction of load introduction was feasible due to low influence on the deflection of the inserts area.

The insert was modeled as a 3D solid with isotropic material properties. Reduced integration, quadratic 20-node hexahedral elements (C3D20R) were used for the meshing of the insert as well as for the laminate. The focus of this work lies on the research and validation of the deformation of the insert depending on the force/displacement-curve of the pull-out test. Therefore, the model developed here is exclusively for prediction of the insert deformation. Hence, the convergence study of (Fig. 7 a) was applied comparing the force/displacement-curves with a different amount of total elements. Furthermore, the number of elements on the horizontal axis of the insert (half of the insert's diameter) is indicated in brackets. As can be seen in (Fig. 7 a), 4024 elements showed good results for further simulation; the corresponding mesh is shown in (Fig. 7 b).

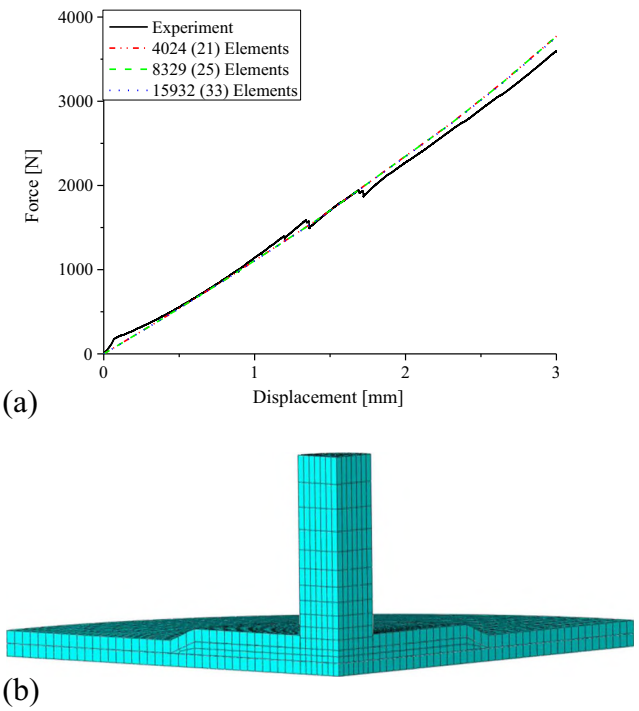

Fig. 7 **(a)** Convergence study of the composite showing good results using 4024 elements **(b)** Meshing of the composite using 4024 C3D20R elements

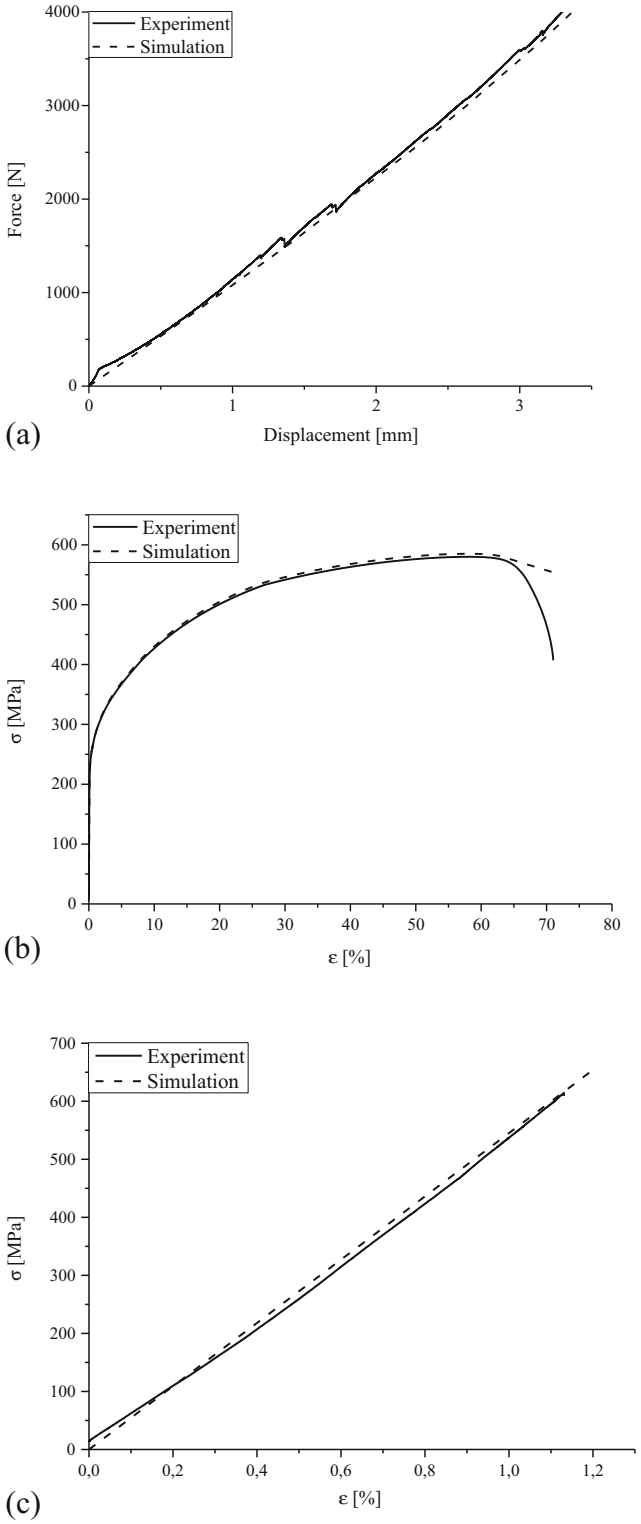

Fig. 8 Comparison of the experimental and simulated test curves of (a) the embedded insert using tie connections (b) the insert's steel (1.4301) and (c) the biaxial CFRP laminate in a quasi-static tensile test

The interface of the isotropic steel insert and laminate was modeled with CB, while the interlaminar CFRP interface between the upper and lower plies was modeled using tie functionality. CB was defined by the damage initiation criterion "maximum stress" and an indication of fracture energy with a linear traction-separation law for failure analysis. The default contact enforcement method was used, where initially only the slave nodes are in contact. Damage initiation was assumed when a maximum contact interaction function that depends on the stress ratio of the coordinate system $\langle n, s, t \rangle$ reaches a value of one.

$$max\left\{\left(\frac{\langle t_n \rangle}{t_n^0}\right),\ \left(\frac{t_s}{t_s^0}\right),\ \left(\frac{t_t}{t_t^0}\right)\right\} = 1 \tag{1}$$

The nominal traction stress vector, $\boldsymbol{t}$, consists of three components representing the normal and the two shear tractions. Brackets $\langle t_n \rangle$ were used to signify that a pure compressive stress state does not initiate damage. For the failure criterion, the values t_n^0, t_s^0 and t_t^0 represent the maximum permissible values for the nominal stress when the deformation is either purely normal to the interface or in the first or the second shear direction, respectively. The material parameters of the resin, steel and carbon fiber were taken from data sheets, but those for the unidirectional layer were calculated using the general mixture rule. The parameters for the damage behavior were taken from experiments (cross tension and shear edge tests) and from the literature (cf. Table 2). The cross tension test was conducted by a normal force introduction on a cut sample consisting of the embedded insert with the CFRP laminate of the same size as the insert. The interface normal strength between the insert and de CFRP laminate was finally determined with the maximum measured force and the area of the insert. The shear edge test is for the determination of the interface (insert/CFRP) shear strength of a cut sample of 20 mm × 10 mm × 3 mm in the area of the embedded insert. Table 2 summarizes the values used for modeling. To validate the model parameters in Table 2, the embedded insert was first simulated using tie connections. The verification of the model material parameters was conducted comparing the experimental and simulated stress/strain curves of the tensile tests. For this purpose, the individual layers of the CFRP were modeled using the solid composite layup functionality with 9375 C3D20R elements and the insert's steel was modeled as a 3D isotropic model with 8399 C3D20R elements. As seen in Fig. 8 a), b) and c), the simulated force/displacement curve and the stress/strain curves resulted in a good fit with the experimental results.

For the first validation of the model, only the deformation of the insert up to the point of the first force decrease (cf. holding point 4) is relevant. Figure 9 a) compares the experimental and simulated pull-out tests up to the displacement of holding point 4. The shape of the test result curves is very similar up to a displacement of 3 mm; after this point, the stiffness of the simulated pull-out test is

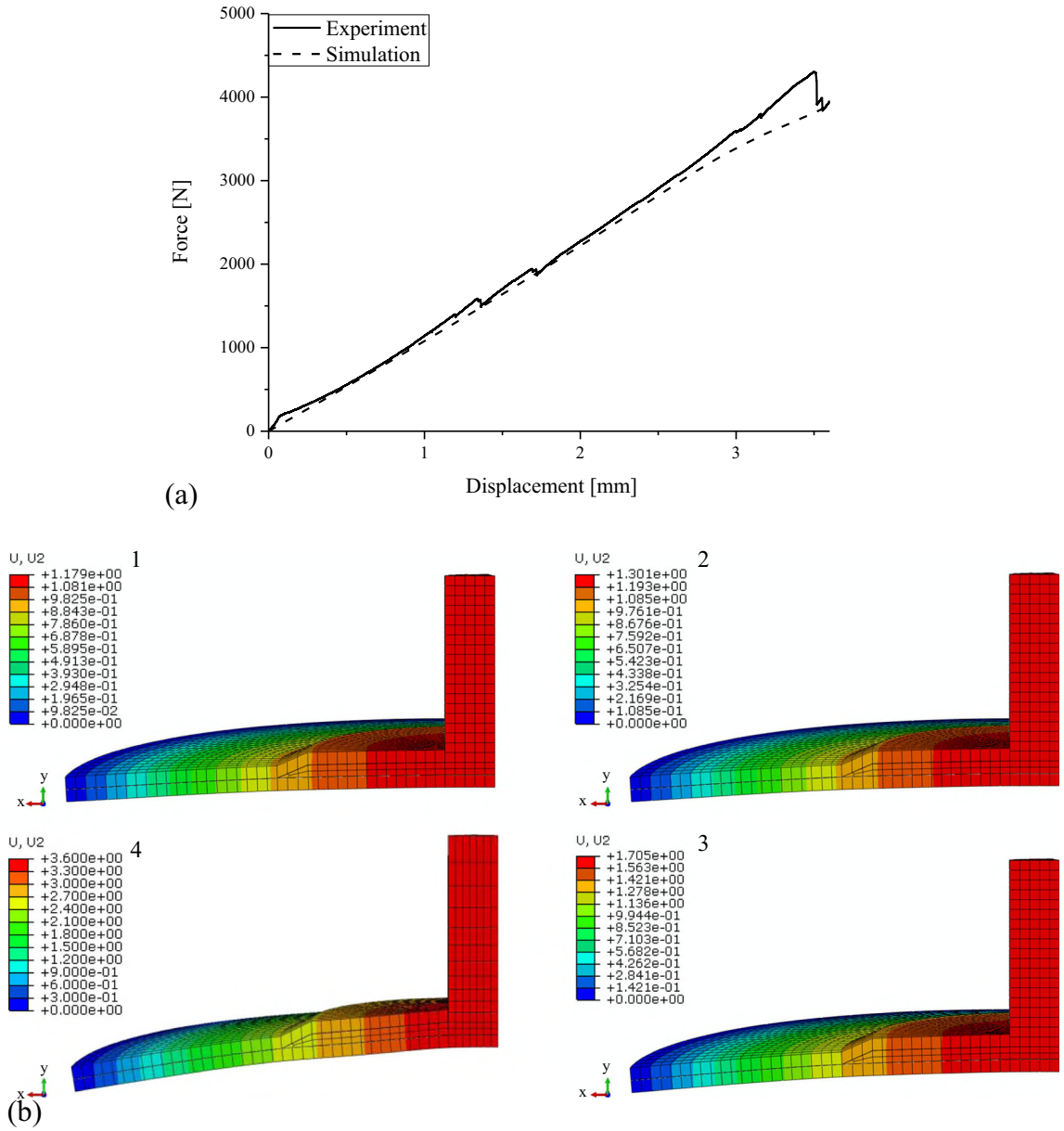

Fig. 9 **(a)** Comparison of the experimental and simulated pull-out tests **(b)** Displacements in the direction of force of the FEM at holding points 1 to 4

reduced due to earlier damage initiation. For validation purposes, the displacement of the insert in ABAQUS® (cf. Figure 9 b)) is compared with the results of the in-situ CT test (cf. Figure 5 c)) for the first four holding points. The model is currently unable to describe the decrease of force due to damage initiation. As shown in Fig. 10 a), the insert deformation in the simulation is only slightly overestimated for the first three displacements. At holding point 4, the modeled insert shows less deformation than the experimental result, although the delamination between the boundary layer and the inserts starts (cf. Figure 10 b)) at the transition stud/base plate. Possible reasons for the deformation discrepancy include the numerical parameter assumptions (e.g., stabilization factor), the material parameter assumptions (cf. Table 2) and the simplification of the hold-down clamp using the boundary condition with constraint in the direction of load introduction.

Discussion

The failure types for the embedded insert under tensile loading coincide with those in [12]. The damage behavior includes fiber breakage around the stud, plastic deformation of the insert based on the co-cured bonding failure, and delamination. The shape of the test curve and the maximum force and deflection match the results in [12]. With the help

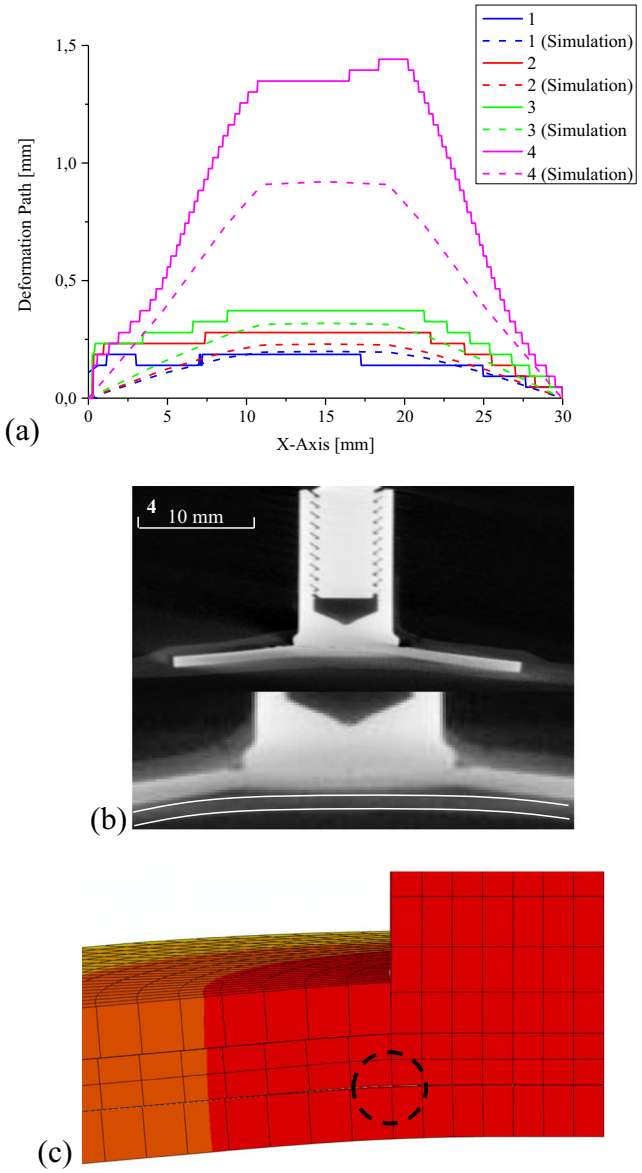

Fig. 10 **(a)** Comparison of experimental and simulated determined deformation path of the insert at holding points 1 to 4; Beginning of delamination of the boundary layer and insert determined by **(b)** CT and **(c)** simulation at holding point 4 (*black* circles)

of the in-situ CT analysis, it is possible to get detailed information about the damage evolution of the laminate and the insert from the measured force. Moreover, it is possible to analyze the deformation path of the insert at certain forces where damage is assumed to occur. The results can be used for validation of a finite element model. The interfaces are modeled with CB, including the maximum stress damage initiation criterion (cf. 1), a common method used for accurate damage prediction in (FRP-) composites and for an accurate representation of the experimental results [28–31]. Comparing the experimental deformation paths of the first four holding points with those of the simulation, it can be concluded that the simulation fits the experiment well. Furthermore, the force/displacement curve of the experimental pull-out test is in acceptable agreement with the simulated test. The shape of the curves of the insert's deformation and the maximum displacement of the study are similar. The discrepancy of 0.5 mm deflection of the insert at holding point 4 could be due to the simplification of the hold-down clamp or due to the assumptions of numerical and/or material parameters. The experiment also shows a higher degree of deformation of the insert, since the shape of the curve tapers down towards the maximum deflection of the stud. Schwarz et al. [10, 11] showed good agreement between the experimental and simulated maximum transmitted force of embedded metal inserts using the tie functionality. Here, it is not possible to learn about the damage behavior or quantitatively analyze the deformation.

Conclusions and Outlook

- In-situ CT analysis was successfully performed under tensile loading to comprehensively investigate damage evolution including insert deformation.
- The damage mechanisms of detachment of the boundary CFRP layer and the insert, fiber fracture and delamination are easily reproduced.
- The deformation of the insert was calculated by extracting a line plot in the center of the insert using MATLAB®.
- Validation of a quarter-section model of ABAQUS® was performed, comparing the deformation path of the insert with the force/displacement curve.

As a focus of future research, the numerical assumptions (e.g., stabilization factor) and material parameters will be analyzed to obtain improved force/displacement curve results up to the point of final failure, including a comparison of the experimental and simulated maximum transmitted force. In addition, the insert's deformation at all holding points should be evaluated to complete the FE analysis by implementing failure mechanisms such as fiber breakage and delamination. Furthermore, the model could be enhanced using CEs or by considering residual process stresses based on the different thermal expansion behaviors of steel and CFRP. An important issue here is the implementation of the interface CFRP/CFRP behavior. Therefore, a convergence study of stress is needed in the interface area for estimation of local stress concentrations leading to delamination within the laminate. The next step to improve the simulation is the modelling of the hold-down clamp including the CFRP square plate to describe real damage behavior.

Acknowledgements This paper is based on investigations of Subproject 3, "Fundamental research of intrinsically produced FRP-metal composites – from embedded insert to load bearing hybrid

structure”- of the priority program 1712 “Intrinsic hybrid composites for lightweight load-bearings”, which is kindly supported by the German Research Foundation (DFG). The authors kindly acknowledge the Institute for Production Science (wbk) of KIT for the manufacturing of the specimen in cooperation with the above-mentioned subproject.

References

1. Camanho PP, Lambert M (2006) A design methodology for mechanically fastened joints in laminated composite materials. Compos Sci Technol 66(15):3004–3020
2. Ueda M, Miyake S, Hasegawa H, Hirano Y (2012) Instantaneous mechanical fastening of quasi-isotropic CFRP laminates by a self-piercing rivet. Compos Struct 94 (11), S. 3388–3393
3. Falconieri D, Franco F (2015) The effect of titanium insert repairs on the static strength of CFRP coupons and joints. Compos Struct 134, S. 799–810
4. Kolesnikov B, Herbeck L, Fink A (2008) CFRP/titanium hybrid material for improving composite bolted joints. Compos Struct 83 (4), S. 368–380
5. Mara V, Haghani R, Al-Emrani M (2015) Improving the performance of bolted joints in composite structures using metal inserts. J Compos Mater 50(21):S. 3001–3018
6. Gebhardt J, Fleischer J (2014) Experimental investigation and performance enhancement of inserts in composite parts. Procedia CIRP 23, S. 7–12
7. Ferret B, Anduze C, Nardari C (1998) Metal inserts in structural composite materials manufactured by RTM. Compos Part A (29), S. 693–700
8. Hopmann C, Fecher ML, Lineman L, Bastian R, Gries T, Schnabel A, Greb C (2013) Comparison of the properties of Onserts and inserts for a high volume production of structural composite parts. Int J Plast Technol 9 (4), S. 179–206
9. Fleischer J, Gebhardt J (2013) Experimental investigation of metal inserts embedded in composite parts manufactured by the RTM process
10. Schwarz M, Magin M, Peil C, Schürmann H (2004) Thin-walled FRP-laminates and local bending moments - incompatible or solvable by a skillful design?
11. Schwarz M, Schürmann H, Fickel M, Magin M, Peil C (2007) Designing of punctual joints acting in fibre-reinforced plastics. Konstruktion 6, S. 90–96
12. Gebhardt J, Pottmeyer F, Fleischer J, Weidenmann K (2015) Characterization of metal inserts embedded in carbon fiber reinforced plastics. MSF 825-826, S. 506–513
13. Stoessel R, Kiefel D, Oster R, Diewel B, Llopart Prieto L (2011) µ-computed tomography for 3D porosity evaluation in carbon fiber reinforced plastics (CFRP)
14. Schell J, Renggli M, van Lenthe GH, Müller R, Ermanni P (2006) Micro-computed tomography determination of glass fibre reinforced polymer meso-structure. Compos Sci Technol 66 (13), S. 2016–2022
15. Tan KT, Watanabe N, Iwahori Y (2011) X-ray radiography and micro-computed tomography examination of damage characteristics in stitched composites subjected to impact loading. Compos Part B 42 (4), S. 874–884
16. Nouri H, Lubineau G, Traudes D (2013) An experimental investigation of the effect of shear-induced diffuse damage on transverse cracking in carbon-fiber reinforced laminates. Compos Struct 106, S. 529–536
17. Ireman T, Ranvik T, Eriksson I (2000) On damage development in mechanically fastened composite laminate. Compos Struct 49, S. 151–171
18. Dietrich S, Weidenmann K, Elsner P (2014) 3D tomographic characterization of sandwich structures. NDT&E Int 62, S. 77–84
19. Elliott JA, Windle AH, Hobdell JR, Eeckhaut G, Oldman RJ, Ludwig W. et al (2002) In-situ deformation of an open-cell flexible polyurethane foam characterised by 3D computed tomography. J Mater Sci 37, S. 1547–1555
20. Adrien J, Maire E, Gimenez N, Sauyant-Moynot V (2007) Experimental study of the compression behavior of syntactic foams by *in situ* X-ray tomography. Acta Mater 55, S. 1667–1679
21. Hufenbach W, Böhm R, Gude M, Berthel M, Hornig A, Ručevskis S, Andrich M (2012) A test device for damage characterisation of composites based on *in situ* computed tomography. Compos Sci Technol 72 (12), S. 1361–1367
22. Scott, A. E.; Mavrogordato, M.; Wright, P.; Sinclair, I.; Spearing, S. M.: *In situ* fibre fracture measurement in carbon–epoxy laminates using high resolution computed tomography. Compos Sci Technol 71 (12), S. 1471–1477, 2011
23. Moffat, A. J.; Wright, P.; Helfen, L.; Baumbach, T.; Johnson, G.; Spearing, S. M.; Sinclair, I.: *In situ* synchrotron computed laminography of damage in carbon fibre–epoxy [90/0]s laminates. Scr Mater 62 (2), S. 97–100, 2010
24. Wright, P.; Fu, X.; Sinclair, I.; Spearing, S. M.: Ultra high resolution computed tomography of damage in notched carbon fiber–epoxy composites. J Compos Mater 42 (19), S. 1993–2002, 2008
25. Toda, H.; Maire, E.; Yamauchi, S.; Tsuruta, H.; Hiramatsu, T.; Kobayashi, M.: *In situ* observation of ductile fracture using X-ray tomography technique. Acta Mater 59 (5), S. 1995–2008, 2011
26. Chateau, C.; Gélébart, L.; Bornert, M.; Crépin, J. Boller, E.; Sauder, C.; Ludwig, W.: *In situ* X-ray microtomography characterisation of damage in SiCf/SiC minicomposites. Compos Sci Technol 71, S. 916–924, 2011
27. Miguélez, M. H.; Zaera, R.; Molinari, A.; Cheriguene, R.; Rusinek, A.: Residual stresses in orthogonal cutting of metals. J Therm Stresses 32 (3), S. 269–289, 2009
28. Chandra, N.: Analysis of interfacial behavior in MMCs and IMCs by the use of thin-slice push-out tests. Compos Sci Technol 54 (1), S. 87–100, 1995
29. Aymerich, F.; Dore, F.; Priolo, P.: Prediction of impact-induced delamination in cross-ply composite laminates using cohesive interface elements. Compos Sci Technol 68 (12), S. 2383–2390, 2008
30. Al-Zand AW, Hamidon W, Badaruzzaman W, Mutalib AA, Hilo SJ (2015) Modelling the delamination failure along the CFRP-CFST beam interaction surface using different finite element techniques. J Eng Sci Technol, S. 1–15
31. Kapidžić, Z.; Ansell, H.; Schön, J.; Simonsson, K.: Quasi-static bearing failure of CFRP composite in biaxially loaded bolted joints. Compos Struct 125, S. 60–71, 2015
32. Reeb, A.; Walter, V.; Schulze, V.; Weidenmann, K.: Characterization of a hybrid Al2O3-aluminum matrix composite manufactured via composite extrusion. J Compos Mater 50 (8), S. 1099–1108, 2016
33. Kuramato, T.; Ohshita, M.; Maeda, K.; Ueda, Y.: Sharpening of an energy band of diagnostic x-ray spectrum with metal filters. IFMBE Proc 14 (3), S. 1533–1536, 2006
34. Barbero EJ (2013) Finite element analysis of composite materials using Abaqus: CRC Press,Taylor & Francis Group (Composite materials, design and analysis)
35. Schön, J.: Coefficient of friction and wear of a carbon fiber epoxy matrix composite. Wear 257 (3–4), S. 395–407, 2004
36. Both JC (2014) Tragfähigkeit von CFK-Metall-Laminaten unter mechanischer und thermischer Belastung. Dissertation. Technische Universität München, München. Lehrstuhl für Leichtbau
37. Zinn, C.; Schaper, M.; Serna, J.; Meiners, D.; Wang, Z.; Troester, T. et al.: Shear edge tests: a benchmark in investigating the influence of different surface pretreatment methods on the shear stress of intrinsically manufactured metal-CFRP hybrids. Int J Autom Compo 2 (3/4), S. 244–271, 2016